LAWRENCE
LIVERMORE
NATIONAL
LABORATORY

LLNL-PROC-425116

Comprehensive Characterization of Voids and Microstructure in TATB-based Explosives from 10 nm to 1 cm: Effects of Temperature Cycling and Compressive Creep

T. M. Willey, L. Lauderbach, F. Gagliardi, B. Cunningham, K. T. Lorenz, J. R. I. Lee, T. van Buuren, R. Call, L. Landt, G. Overturf

March 5, 2010

14th International Detonation Symposium
Coeur d'Alene, ID, United States
April 11, 2010 through April 16, 2010

Disclaimer

Comprehensive Characterization of Voids and Microstructure in TATB-based Explosives from 10 nm to 1 cm: Effects of Temperature Cycling and Compressive Creep

Trevor M. Willey, Lisa Lauderbach, Franco Gagliardi, Bruce Cunningham, K. Thomas Lorenz, Jonathan R. I. Lee, Tony van Buuren, Robert Call[a], Lasse Landt[b], and George Overturf

Lawrence Livermore National Laboratory, 7000 East Avenue, Livermore, CA 94550
[a]current address: Utah State University, 4415 Old Main Hill, Logan, UT 84322-4415
[b]current address: Technische Universität Berlin, Hardenbergstr. 36, 10623 Berlin, Germany

This paper outlines the characterization of voids and Microstructure in TATB-based Explosives over several orders of magnitude, from sizes on the order of 10 nm to about 1 cm. This is accomplished using ultra small angle x-ray scattering to investigate voids from a few nm to a few microns, ultra small angle neutron scattering for voids from 100 nm to 10 microns, and x-ray computed microtomography to investigate microstructure from a few microns to a few centimeters. The void distributions of LX-17 are outlined, and the microstructure of LX-17 is presented. Temperature cycling and compressive creep cause drastically different damage to the microstructure. Temperature cycling leads to a volume expansion (ratchet growth) in TATB-based explosives, and x-ray scattering techniques that are sensitive to sizes up to a few microns indicated changes to the void volume distribution that had previously accounted for most, but not all of the change in density. This paper presents the microstructural damage larger than a few microns caused by ratchet growth. Temperature cycling leads to void creation in the binder poor regions associated with the interior portion of formulated prills. Conversely, compressive creep causes characteristically different changes to microstructure; fissures form at binder-rich prill boundaries prior to mechanical failure.

Introduction

TATB (1,3,5-triamino-2,4,6-trinitrobenzene) is a highly insensitive energetic material. Understanding initiation, detonation, and mechanical properties of LX-17, a TATB-based polymer-bound explosive (PBX) requires a comprehensive understanding of the voids and microstructure, spanning length scales from nanometers to centimeters. Such structural data feeds into the combination of experiment and modeling. For example, at smaller sizes, current hot-spot models suggest that voids (pores) with sizes between about 100 nm and few microns in these materials affect initiation and detonation properties. Experimental void size distributions are thus important to compare to detonation properties and as empirical input to hot-spot models of initiation and detonation[1, 2]. At larger size regimes around 1 mm, LX-17 has a

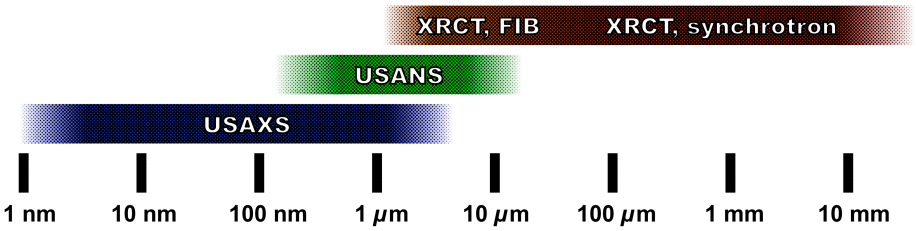

Figure 1: A summary of the techniques used to comprehensively characterize TATB-based explosives over feature sizes spanning six orders of magnitude.

heterogeneous microstructure. Nominally, LX-17 consists of about 7.5% binder and 92.5% TATB; in reality, on a mm scale, TATB-rich areas have only about 5.1% binder and 2.0% void, while binder rich areas have 8.3% binder and 1.0% void[3]. Work is progressing to understand how this heterogeneous microstructure affects both mechanical and detonation properties. This study presents a comprehensive characterization of LX-17, and also presents how temperature cycling and compressive creep change the microstructure. These data provide experimental empirical data for input into models of initiation and detonation, and give insight into mechanisms for mechanical failure, improving future TATB-based PBX materials.

Experimental

Understanding voids and microstructure over the wide range of length scales requires integrating multiple methods; we use ultra-small angle x-ray scattering (USAXS), ultra-small angle neutron scattering (USANS), and x-ray computed microtomography. Using this combination of techniques we are able to investigate structure spanning several orders of magnitude in size from a few nanometers to a few centimeters, as summarized in figure 1. Void size distributions derived from USAXS and USANS range over a few nm to a few microns. Computed microtomography determines compositional heterogeneity and larger defects from microns to centimeters. These techniques are used to quantitatively characterize TATB-based explosives, in particular, LX-17.

USAXS and USANS

Ultra small angle x-ray scattering data were acquired at the USAXS endstation at the Advanced Photon Source, Argonne National Laboratory, Argonne, Illinois[4]. This Bonse-Hart system can measure scattering vectors (q) from about 10^{-4} $Å^{-1}$ to 1 $Å^{-1}$. The monochromator was positioned at about 11 keV photon energy, and data were reduced using the codes developed for this USAXS instrument, including absolute scattering intensity calibration and slit desmearing[5].

Ultra small angle neutron scattering measurements were performed at the Perfect Crystal Diffractometer for Ultra Small-Angle Neutron Scattering at the National Center for Neutron Research, National Institute of Standards and Technology, Gaithersburg, Maryland[[6, 7]. Data were acquired on samples mounted in Cd windows 1.59 cm in diameter, and were reduced using the integrated software package[7].

Inhomogeneities in electron density (USAXS) or nuclear makeup and density (USANS) give rise to small angle x-ray scattering. The scattering contrast between TATB and Kel-F 800 binder is minimal: for 11 keV x-rays, the contrasts are about 16.6 x 10^{10} cm^{-2} for TATB and 17.5 x 10^{10} cm^{-2} for Kel-F 800, and for the neutrons, the contrast is about 4.9 x 10^{10} cm^{-2} and 4.4 x 10^{10} cm^{-2} for TATB and Kel-F 800 respectively. Thus, voids are the primary source of scattering. Although the scattering contrast difference between TATB and Kel-F 800 is larger with neutrons than with x-rays, the contrast still similar enough to conclude that voids are the main cause of scattering. In fact, if one assumes the neutron scattering in LX-17 comes from the minority Kel-F 800 phase, rather than voids, using the scattering

contrast between TATB and Kel-F 800, an unphysical result for the Kel-F volume fraction (>45%) ensues. Void size distributions, assuming uncorrelated voids, were derived from the scattering using the maximum entropy method, implemented in the Irena package for SAS data analysis[5]. The implementation for TATB-based explosives has been described previously[1, 2, 8].

Computed Tomography

Two types of tomography were used to image the samples. High-resolution tomography was performed using an instrument designed primarily for Focused Ion Beam (FIB) processes. The x-ray tomography portion of the instrument is a point projection SEM hosted x-ray system, with an electron beam spot size of ~2 nm using an electron gun energy of 20 kilovolts, and a platinum target with a prominent K-line at 9.44 keV. The images were recorded on a 1340 x 1300 CCD array with pixel size of 20 by 20 microns. The source to detector distance was 211 mm, while the source to sample distance was set to 2.64 millimeters, leading to camera pixels representing about 0.25 by 0.25 microns each at the CCD detector. Views were acquired at 1-degree increments through 360 degrees. The reconstruction was performed using proprietary software provided by the manufacturer (Gatan, Inc., Pleasanton, California).

The presented synchrotron based tomography data were acquired at beamline 8.3.2 at the Advanced Light Source, Lawrence Berkeley National Laboratory[9], using a photon energy of 20 keV. X-rays of 25 and 30 keV were also used to determine composition. Every 20 views, bright field images were acquired to normalize incident x-ray flux and changes in the delivered synchrotron x-ray flux at the detector; dark field images were also acquired. The transmitted x-rays impinge upon a $CdWO_4$ single crystal scintillator, and are recorded by a Cooke PCO 4000 CCD camera. In order to minimize phase effects, the camera and scintillator box are moved as close as possible to the specimen, resulting in a distance of about 7 cm between sample and scintillator. Auxiliary data were also acquired at beamline BM2 at the Advanced Photon Source[10].

Tomographic slices were reconstructed via filtered back projection using the LLNL-developed ImageRec code as well as the commercially available Octopus package (Ghent University, Belgium) to retrieve attenuation coefficients μ in units of mm^{-1} and/or cm^{-1} for each voxel within the volume. Attenuation of x-rays through a specimen is described by $I = I_0 \cdot e^{-\mu x}$ where I is the x-ray intensity through a material, I_0 is the initial x-ray intensity, x is the material thickness, and μ is an attenuation coefficient characteristic of the material and dependent upon density. In order to remove ring artifacts from each sinogram, each row was fit with the attenuation expected from a cylinder, and the rows and fits were averaged. This allowed for deconvolution of the x-ray attenuation through the part from artifacts introduced by the detector, scintillator, camera optics, and by inhomogeneous x-ray illumination.

Sample Preparation

LX-17 (nominally 92.5% TATB and 7.5% Kel-F 800 binder) with densities of 1.91 to 1.92 g/cm^3 were obtained by pressing the samples three times at 2.1 x 10^8 Pa (3.0 x 10^4 PSI) for 5 minutes each press, with the pressing die held at 105° C. USAXS and USANS samples were pressed to about 0.8 mm and 1.5 mm thick, respectively. The FIB XRCT samples were pressed to 0.8 mm thick, and then cut with a femtosecond laser[11] to obtain 0.4 mm diameter, 0.8 mm long cylinders. For synchrotron-based tomography studies of microstructure, LX-17 samples were die pressed into 1.27 cm diameter, 2.54 cm long cylinder samples. Between measurements of pre-and post ratchet growth, the sample was conditioned by cycling 30 times over a range of -54 to +76˚C. The per-cycle time was approximately four hours, with the specimen dwelling at each temperature extreme for a minimum of forty minutes. Measurements performed using immersion density techniques indicate that the sample used in this study decreased in density by 1.4%.

The specimen used to study compressive creep was placed under 600 PSI (4.1 x 10^6 Pa) uniaxial stress for approximately 430 hours at 70 ˚C. It was then allowed to recover. With the exception of some friction at the specimen ends there was no lateral confinement. As a result, the specimen experienced approximately 13000

microstrain in creep followed by approximately 3000 microstrain recovery, for a net permanent axial strain of roughly 10,000 microstrain. The overall consequence of conditioning process was a reduction in cylinder height, accompanied by lateral growth and a reduction in density of 0.5%.

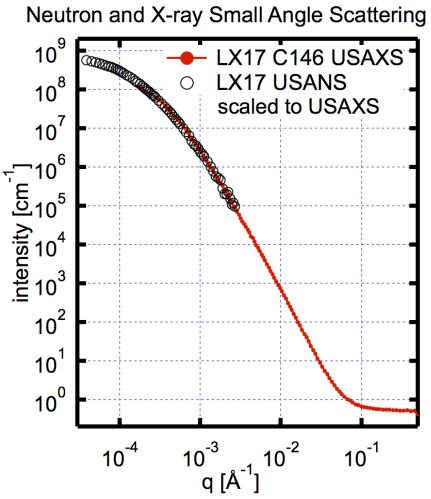

Figure 2: Ultra small angle x-ray scattering (solid line) and ultra small angle neutron scattering (open circles) data for LX-17. The neutron data has been scaled to match the x-ray data. The scattering has a broad Guinier region from below 10^{-4} to about 10^{-3} Å^{-1}, and a power law slope of approximately -4 in the 10^{-3} Å^{-1} to 10^{-2} Å^{-1} range.

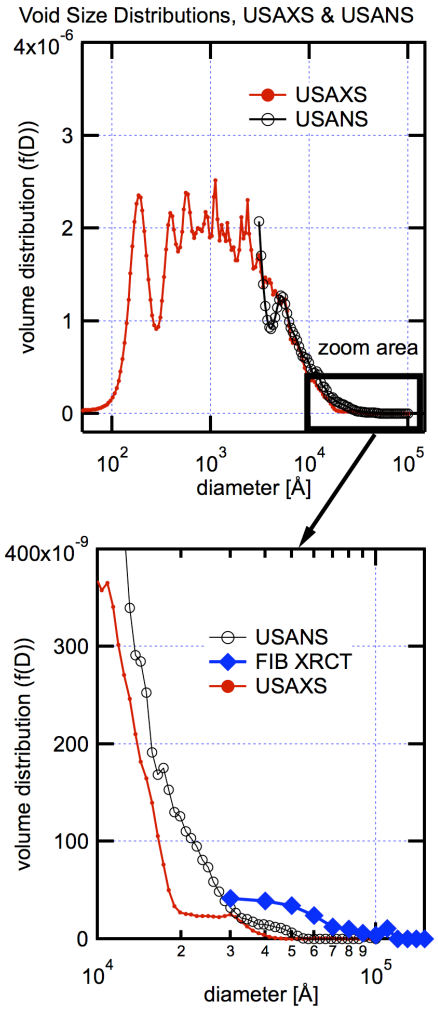

Figure 3: Derived size distributions from the USAXS (solid) and USANS (open circles) in the top pane, with an inset of sizes from 1 to 11 microns in the lower pane. The bottom pane includes the void distribution from a very small tomographically reconstructed volume.

Results and Discussion

Figure 2 presents the USAXS and USANS data together from the same pristine LX-17 sample acquired at different times. The USANS data has been scaled to match the USAXS data for clarity; generally neutrons have a different scattering contrast than the x-rays. The small angle scattering has a well-defined Guinier region from below 10^{-4} to about 10^{-3} Å^{-1}. This region indicates a size regime for voids scattering x-rays and/or neutrons, and is the primary contributor to the size distributions presented in figure 3. The scattering also possesses a power law slope of approximately -4 in the 10^{-3} to 10^{-2} Å^{-1} range of the log-log plot of scattering as presented in the figure. This is not uniquely associated with, but does indicate the scatterers giving rise to the Guinier are generally three dimensional, i.e. more spherical than disk-like (2 dimensional) or rod-like (1 dimensional) in shape. Finally, the scattering dips into the instrumental background somewhere in the regime

just less than 10^{-1} Å^{-1}; however, there is a small second Guinier in this q-range that is augmented during temperature cycling[2].

The upper pane of figure 3 presents the derived void size distributions from the USAXS and USANS data in figure 2[1-3, 12]. TATB-based materials, especially those with Kel-F 800 binder like LX-17 and PBX-9502[13], have a bimodal, log-normal void size distribution. According to the scattering, voids from a few nanometers to about 10 microns comprise about 1.3% of the volume. The lower pane is an expanded area of the upper pane, from about 1 to about 15 microns. Again, size distributions derived from both USAXS and USANS are presented; USANS detects incrementally more voids through this region. USAXS shows 0.2% of the voids are larger than 1 micron, and less than 0.1% larger than 2 microns, while USANS shows that 0.4% are larger than 1 micron, and 0.1% larger than 2 micron. We also plotted the void distribution obtained from the FIB based CT system on a very small, 0.4 mm diameter and 0.8 mm tall cylinder where voids were counted in an inscribed rectangular volume of 250 microns by 250 microns by 430 microns. Voids were counted by looking for voids sufficiently close to zero with connectivity to other similar voxels; diameters of these voids were estimated through the simple relation for spherical particles, i.e. $d = \sqrt[3]{6V/\pi}$. Although simplistic, this is analogous to the method used for scattering techniques, in that a form factor for spheres is assumed. The integrated volume of pores obtained on this small area with tomography, of voids ~ 3 microns and larger, is about 0.4% of the total volume. This void volume is slightly less than, and matches, perhaps fortuitously well, the roughly 0.5% void volume not accounted for using USAXS. Previously, on a number of different samples, USAXS accounted for about 1.5% of the voids determined with density measurements to be 2.0%[1]. In this small sample, voids 3-15 microns make up nearly 0.4% of the volume. Although this is a remarkable match, there are weaknesses in the methods used for this estimation. First, the small, inscribed volume may not be completely representative of bulk LX-17, especially given the variations in composition on the 1 mm scale presented later in this report. Voxel counting is not particularly accurate due to phase effects in the imaging and uncertainty for boundary locations. Further, this sample was a separate pressing, known to cause some variation, while USANS and USAXS presented here were from exactly the same sample. Even with these experimental uncertainties, this technique allows us to image voids with sizes from a few microns to a few 10's of microns, and despite the small sampling, their volume does capture and represent a significant portion of the voids not accounted for when using scattering techniques.

Figure 4 presents a 3 dimensional breakdown of the constituents of LX-17 based on data acquired with monochromatic x-rays from a synchrotron source. Multiple datasets of pristine material, acquired at different monochromatic photon energies, can be used to quantitatively determine constituent volume fractions, voxel by voxel, in a three dimensional volume. Quantitative CT reconstructions return linear attenuation coefficients for each voxel; each acquisition leads to a linear equation relating volume fractions and linear attenuation coefficients of the constituents a, b, and c, i.e.

$$V_a \cdot \mu_a + V_b \cdot \mu_b + V_c \cdot \mu_c = \mu_{measured}$$

where the attenuation coefficients are a function of energy, and the volume fractions must add to 1.

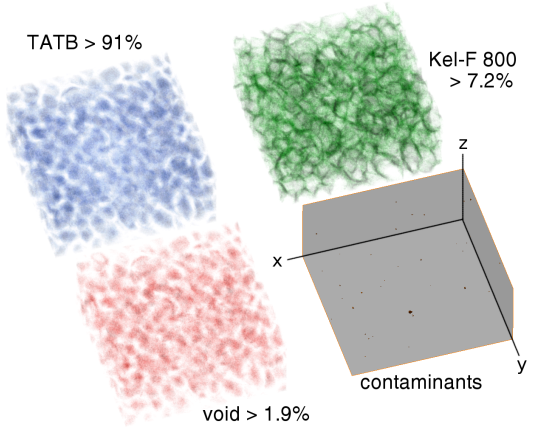

Figure 4: Three-dimensional representation of the concentration of major constituents of LX-17 derived from the CT reconstruction. The volume is 7.1 mm x 7.1 mm x 3.2 mm.

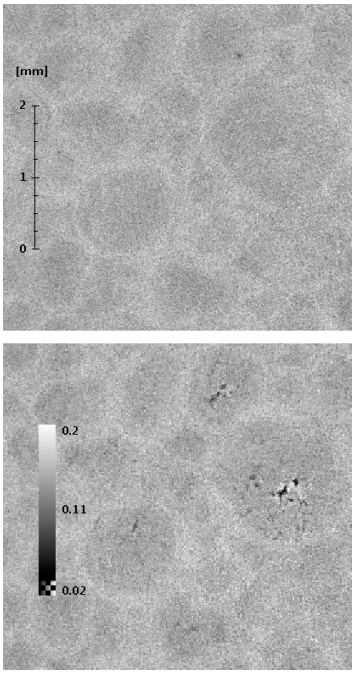

Figure 5: CT slice of pristine LX-17 (top), and the same area in the same sample after temperature cycling and ratchet growth (bottom). The damage large enough to be detected with CT occurs in the binder-poor prill interiors.

Atomic attenuation coefficients are well tabulated[14-16]. An iterative process, adjusting effective photon energy to obtain measured density for the imaged parts was used to derive constituent volume fractions with acquisitions at 3 different energies.

As described previously[3], LX-17 has a heterogeneous microstructure with Kel-F 800 binder-rich boundaries surrounding TATB and void-rich interiors. This is a result of the formulation of LX-17: as the binder and TATB are mixed, mm sized spheres, or "prills", form. Apparently, the surfaces of these prills retain a higher concentration of binder than the interiors, even when pressed into shape at elevated temperature. The variation in composition ranges from an average of 5.9% binder and 2.0% void in the interiors, to an average of 8.5% binder and 1.0% void in binder rich regions. Additionally, higher atomic weight contaminants are present in LX-17 and encompass ~0.1% of the volume. Although not the focus of this work, the attenuation in several of these small particles is consistent with either silicates/sand or metals/steel/rust. The volume, obtained by converting the reconstructed x-ray attenuation values into relative concentration, is now being used as empirical experimental input to computational modeling of microstructural heterogeneity on shock response and detonation properties[17].

How ratchet growth affects void distributions from a few nm to a few microns has been studied extensively, but little is known about how physical insults, namely temperature cycling and ratchet growth, as well as compressive creep, affect the larger microstructure of LX-17. The damages are drastically different.

Ratchet growth refers to the irreversible growth that occurs in compacted TATB-based explosives when they are thermally cycled. It is common for materials, in general, to expand volumetrically when heated and then return to their original state when cooled. TATB based compactions also expand when heated and shrink when cooled. However, during especially the first few temperature cycles TATB based compactions do not return to their original state but retain some of the growth that occurred during heating. The consequence of ratchet growth is both a permanent net increase in part size and a permanent decrease in part density.

Ratchet growth is believed to be associated with the highly anisotropic thermal expansion behavior of individual TATB crystals. The c-axis of TATB crystals expands more than an order of magnitude more than directions orthogonal to the c-axis[18]. When heated and cooled, the crystals themselves do not experience permanent growth. However, compactions consisting of many randomly oriented crystals in a binder matrix exhibit the behavior described. LX-17 and PBX-9502 (nominally 7.5% and 5% Kel-F 800 binder, respectively) are common examples of TATB based explosives that exhibit this irreversible volume expansion.

In a compaction, ratchet growth may be isotropic or distinctly anisotropic, depending on the manner in which the material is pressed. Compaction processes that generate uniform stress fields tend to create materials that are relatively

non-directional. Simple billet pressing techniques using hydrostatic fluids will, on average, produce material that is less directional than, for example, die and plunger compactions that often result in pressings that show strong preferential growth. The directionality that is present in TATB based compactions may likely be due to statistically based crystal orientation processes that occur during densification.

Unless the material has been previously temperature cycled extensively, i.e., "cycled out", completely unconfined TATB-based PBXs experience some permanent growth in all directions when exposed to temperature fluctuation. Since the mass and density of the constituents (i.e. TATB and binder) remain essentially constant, the overall volumetric growth and density reduction lead to void creation. The total void volume created is a function of a variety of factors, including the material's initial density, the temperature range over which cycling occurred, and the number of cycles to which the material was subjected. For a fixed temperature range, expansion will be expected to approach a maximum after 30 to 40 cycles.

In specimens that have undergone ratchet growth, scattering techniques show that during temperature cycling, the log-normal void volume distribution, in the 10 nm to micron regime, shifts towards more prevalent voids with larger sizes[1, 2, 12]. These void volume distributions derived from USAXS and USANS account for the majority, but not all of the volume expansion[1], leading one to conclude that damage also occurs at sizes larger than the sensitivity limit of USAXS or USANS. Figure 5 presents two views of the same 18 micron thick XRCT slice, before (top) and after (bottom) ratchet growth. Large voids and fissures appear at the binder-poor interiors, and are somewhat similar in morphology to under-pressed samples[12].

In stark contrast to the morphology of ratchet growth, figure 6 presents the microstructure of a 4 mm section out of the center of a 12.7 mm (½") diameter and 25.4 mm (1") tall LX-17 specimen that had undergone unconfined compressive creep. This specimen was placed under 600 PSI (4.1 x 10^6 Pa) uniaxial stress for approximately 430 hours at 70 ˚C and then allowed to recover. An increase in temperature will cause a softening of the binder,

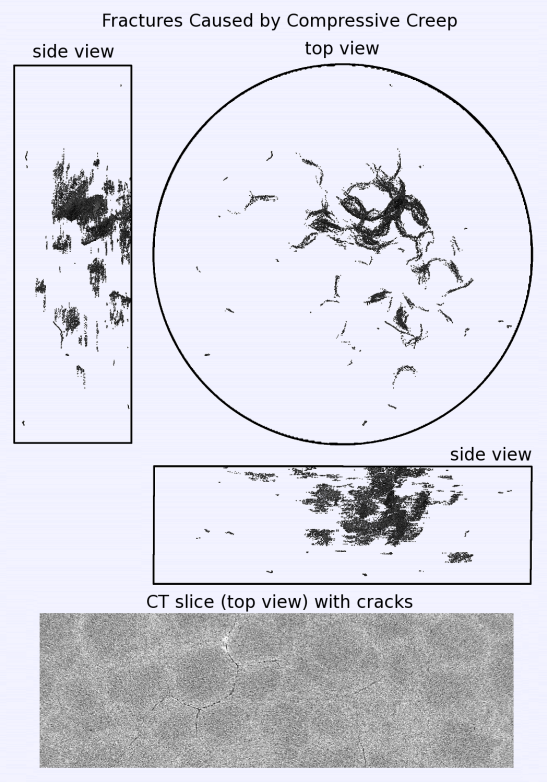

Figure 6: Rendering of cracks present in the central region of an LX-17 cylinder after compressive creep.

leading to an increase in creep rates overall. With creep, the extent of potential damage is not limited, but, under ongoing loading, may proceed until the strain rate accelerates and specimen failure ensues. Typically, for LX-17 cylinders of this size under uniaxial creep, we may expect to see the failure process (as evidenced by an increasing strain rate) begin at about 20,000 microstrain. Axial strains may be expected to reach 3-4% or greater prior to fracture and specimen collapse.

The specimen used for Figure 6 experienced approximately 2/3 of the strain at which we would expect onset of mechanical failure. The overall consequence of conditioning process was a reduction in cylinder height, accompanied by lateral growth and a reduction in density of 0.5%.

Figure 6 presents the microstructural damage caused by extreme compressive creep. Fissures appear along binder-rich prill boundaries, the

opposite of the damage caused by temperature cycling. The bottom pane presents a CT slice representation of this microstructure. To better understand the morphology, three views of the 4 mm high section out of the central portion of the 25 mm tall cylinder are presented in the balance of the figure. The fissures in this central region have a preferred geometry; they generally run vertically in the cylinder around prill particles, with few horizontal fissures. The specimen experienced a reduction in length, and consequently the volumetric expansion that occurred took place in the radial direction in the imaged central region. Given these dynamics during creep, fracturing tends to occur with separations opening vertically, as is seen in the figure. Generally, after specimen collapse, there is often visible evidence of fractures that occur at prill interfaces. The extent to which prill-to-prill separation is present varies and depends on the quality of the adhesion and intermixing at the prill bounderies that took place during compaction. For example compaction at low temperatures will often result in poor prill-to-prill adhesion. This particular cylinder, however, was pressed at 105 C, a temperature commonly used for TATB / Kel-F 800 formulations, but demonstrates that crack initiation occurs at prill boundaries.

Compressive creep, prior to mechanical failure, causes crack initiation and propagation at prill boundaries, indicating potential pathways for improving mechanical strength[12]. These combined data are an important step to understanding microstructural mechanisms that affect mechanical properties, provide a comprehensive characterization of the structure from nanometers to centimeters that can be used as empirical input to computational models of detonation, and assist in determining the relationship between voids and microstructure to detonation properties.

Conclusions

A combination of USAXS, USANS, and x-ray computed tomography has been used to characterize voids and microstructure in LX-17, a TATB-based explosive with 7.5% Kel-F 800 binder. LX-17 and other TATB-based explosives generally have a bimodal log-normal size distribution, with 10 nm small voids, and a broad distribution of larger voids centered at several hundred nm and extending into the micron size range. LX-17 has a heterogeneous microstructure with binder-rich boundary areas surrounding void and TATB-rich regions. Constituent volume fractions generated from multiple-energy monochromatic x-ray CT reconstructions are used as empirical input for models of shock response, initiation and detonation. The two insults studied, temperature cycling / ratchet growth and compressive creep, cause drastically different changes to microstructure. Temperature cycling opens larger voids at TATB and void-rich prill interiors, while compressive creep initiates columnar fissures at binder-rich prill boundaries.

Acknowledgements

The authors thank John Kinney, Nick Teslich, Keo Springer, Gary Friedman, and Dan Scheberk (LLNL); Alastair MacDowell, Eric Schaible, and James Nasiatka (LBNL); John Barker (NIST); and Francesco de Carlo and Jan Ilavsky (Argonne NL). This work performed under the auspices of the U.S. Department of Energy by Lawrence Livermore National Laboratory under Contract DE-AC52-07NA27344. Use of the Advanced Photon Source and the Advanced Light Source are supported by the U. S. Department of Energy, Office of Science, Office of Basic Energy Sciences, under Contracts DE-AC02-06CH11357 and DE-AC02-05CH11231, respectively. This work used neutron research facilities at the National Institute of Standards and Technology, U. S. Department of Commerce, supported by the National Science Foundation under Agreement No. DMR-0454672.
LLNL-PROC-425116

References

1. T.M. Willey, J. Handly, B.L. Weeks, T. van Buuren, J. Ilavsky, J.R.I. Lee, G.E. Overturf, and J.H. Kinney, "Changes in Pore Size Distribution upon Thermal Cycling of TATB-based Explosives Measured by Ultra-Small Angle X-ray Scattering",

Propellants, Explosives, Pyrotechnics, Vol. 31, pp. 466-471, 2006.
2. T.M. Willey, D.M. Hoffman, T. van Buuren, L. Lauderbach, J. Ilavsky, R.H. Gee, A. Maiti, G.E. Overturf, and L.E. Fried, "In-Situ Monitoring of the Microstructure of TATB-based Explosive Formulations During Temperature Cycling Using Ultra-small Angle X-ray Scattering", *Propellants Explosives Pyrotechnics*, Vol. 34, pp. 406-414, 2009.
3. J.H. Kinney, T.M. Willey, and G.E. Overturf, "On the Nature of Variations in Density and Composition within TATB-based Plastic Bonded Explosives", *Proceedings of the 13th International Detonation Symposium*. Vol. pp. 388-392, Norfolk, VA, USA, July 23-28, 2006.
4. J. Ilavsky, P.R. Jemian, A.J. Allen, F. Zhang, L.E. Levine, and G.G. Long, "Ultra-small-angle X-ray scattering at the Advanced Photon Source", *Journal of Applied Crystallography*, Vol. 42, pp. 469-479, 2009.
5. J. Ilavsky and P.R. Jemian, "Irena: tool suite for modeling and analysis of small-angle scattering", *Journal of Applied Crystallography*, Vol. 42, pp. 347-353, 2009.
6. J.G. Barker, C.J. Glinka, J.J. Moyer, M.-H. Kim, A.R. Drews, and M. Agamalian, "Design and performance of a thermal-neutron double-crystal diffractometer for USANS at NIST", *Journal of Applied Crystallography*, Vol. 38, pp. 1004, 2005.
7. S.R. Kline, "Reduction and Analysis of SANS and USANS Data Using Igor Pro", *Journal of Applied Crystallography*, Vol. 39, pp. 895, 2006.
8. D.M. Hoffman, T.M. Willey, A.R. Mitchell, and S.C. Depiero, "Comparison of new and legacy TATBs", *Journal of Energetic Materials*, Vol. 26, pp. 139-162, 2008.
9. D. Robin, J. Krupnick, R. Schlueter, C. Steier, S. Marks, et al., "Superbend upgrade on the Advanced Light Source", *Nuclear Instruments & Methods in Physics Research Section a-Accelerators Spectrometers Detectors and Associated Equipment*, Vol. 538, pp. 65-92, 2005.
10. Y.X. Wang, F. De Carlo, D.C. Mancini, I. McNulty, B. Tieman, et al., "A high-throughput x-ray microtomography system at the Advanced Photon Source", *Rerview of Scientific Instruments*, Vol. 72, pp. 2062-2068, 2001.
11. F. Roeske, J. Benterou, R. Lee, and E. Roos, "Cutting and Machining Energetic Materials with a Femtosecond Laser", *Propellants, Explosives, Pyrotechnics*, Vol. 28, pp. 53-57, 2003.
12. T.M. Willey and G.E. Overturf, "Towards Next Generation TATB-based Explosives by Understanding Voids anad Microstructure from 10 nm to 1 cm", *Proceedings of the 40th International Conference of the Fraunhofer Institute for Chemical Technology: Energetic Materials: Characterization Modelling, and Validation*. Vol. pp. V19.1-V19.12, Karlsruhe, Germany, June 23-29, 2009.
13. D.G. Thompson, G.W. Brown, J.T. Mang, R. DeLuca, B. Patterson, and S. Hagelberg, "Characterizing the Effects of ratchet Growth on PBX 9502", *AIP Conference Proceedings, Shock Compression of Condensed Matter 2009*. Vol. 1195, pp. 388-391,
14. B.L. Henke, E.M. Gullikson, and J.C. Davis, "X-Ray Interactions - Photoabsorption, Scattering, Transmission, and Reflection at E=50-30,000 Ev, Z=1-92", *Atomic Data and Nuclear Data Tables*, Vol. 54, pp. 181-342, 1993.
15. *http://physics.nist.gov/PhysRefData/XrayMassCoef/cover.html*.
16. *http://www.cxro.lbl.gov*.
17. *See H. K. Springer et. al., in this volume.*
18. J.R. Kolb and H.F. Rizzo, "Growth of 1,3,5-Triamino-2,4,6-Trinitrobenzene (Tatb) .1. Anisotropic Thermal-Expansion", *Propellants, Explosives, Pyrotechnics*, Vol. 4, pp. 10-16, 1979.